

# On the Manganese Dissolution Process from $\text{LiMn}_2\text{O}_4$ Cathode Materials

Yonas Tesfamhret, Haidong Liu, Zhigang Chai, Erik Berg, and Reza Younesi\*<sup>[a]</sup>

Transition metal (TM) dissolution is a process experienced by most cathode materials based on lithium transition metal oxides. Spinel  $\text{LiMn}_2\text{O}_4$  (LMO) is the best-known cathode material that suffers from TM dissolution. Therefore, LMO is selected here to understand the dissolution process and derive an inductively coupled plasma optical emission spectroscopy (ICP-OES) method for quantifying dissolved metal ions. Furthermore, the LMO powder is coated with thin  $\text{Al}_2\text{O}_3$  films of different thicknesses using atomic layer deposition (ALD) in an attempt to suppress the dissolution of Mn. Two different types of counter electrodes, lithium iron phosphate (LFP) and Li-metal, were used to investigate the role of the counter

electrode on Mn dissolution. HF is identified as the lead cause of Mn dissolution, through comparisons of cells containing  $\text{LiPF}_6$  or  $\text{LiClO}_4$  based electrolytes. The results show that Li-metal counter electrode effectively minimizes the dissolution process via likely consuming HF and  $\text{H}_2\text{O}$  impurity. In contradiction to the purpose of the protective  $\text{Al}_2\text{O}_3$  thin film coating, surface coated LMO showed higher dissolution of Mn compared to pristine LMO, both in LFP || LMO and Li || LMO configurations.  $\text{Al}_2\text{O}_3$  is proposed to generate  $\text{H}_2\text{O}$  when reacts with HF.  $\text{H}_2\text{O}$  could have the possibility to migrate back in the electrolyte and participate in the hydrolysis of  $\text{LiPF}_6$ , resulting in more HF and thereby more Mn dissolution.

## 1. Introduction

Since the introduction of  $\text{LiCoO}_2$  into the battery market, cathode materials based on transition metal oxides and their derivatives have attracted a substantial interest in research and commercial applications.<sup>[1,2]</sup> The transition metals (TMs) in these cathode materials play an important role in aging and safety of lithium ion batteries. Although aging mechanisms of positive electrodes depend on the properties of the specific materials, structural changes during cycling, surface alteration and chemical decomposition/dissolution reactions have been identified among the roots of aging for cathode materials.<sup>[3]</sup> Decomposition/dissolution reactions that result in dissolution of TMs from the cathode cause a direct loss of active material as well as a potential migration of TMs and deposition on the anode surface, which not only alters the cathode surface structure but also induces impedance and negatively affects cyclability.<sup>[4,5]</sup> This dissolution phenomenon is very pronounced especially in  $\text{LiMn}_2\text{O}_4$  (LMO) cathode material. LMO has a spinel crystal structure with space group of  $\text{Fd}\bar{3}m$  where a close-packed oxygen array allocates cations in octahedral and tetrahedral sites.<sup>[6]</sup> The same amount of  $\text{Mn}^{3+}$  and  $\text{Mn}^{4+}$  occupies the octahedral sites while lithium occupies the

tetrahedral sites.<sup>[7,8]</sup> Electrochemical intercalation and deintercalation of Li-ions occurs in the potential range of 3.5–4.3 V vs.  $\text{Li}^+/\text{Li}$ , offering a theoretical specific capacity of 148 mAh/g.


Dissolution of Mn from LMO has been shown to be a result of (i) Jahn-Teller distortion and (ii) subsequent corrosion due to increased electrolyte acidity.<sup>[9–14]</sup> Jahn-Teller effect, which is induced by  $\text{Mn}^{3+}$ , causes a symmetry distortion of the octahedra complex and transforms the spinel into a tetragonal symmetry.<sup>[8,15–17]</sup> This mechanism is more pronounced at high current rates on account of Li-diffusion in the electrolyte being much faster than in the LMO structure, resulting in  $\text{Li}^+$  concentrating more at the surface of LMO particles and forming a  $\text{Mn}^{3+}$  rich region.<sup>[16,18]</sup> It has widely been proposed that disproportionation reaction of the  $\text{Mn}^{3+}$  leads to  $\text{Mn}^{2+}$  dissolving into the electrolyte.




This identified behavior of aging mechanism due to TM dissolution makes LMO a model cathode material in this study for qualitative and quantitative investigation in understanding the underlying mechanisms of TM dissolution process and the related capacity fading.

Tarascon et al. first reported the inferior cyclability of LMO at elevated temperatures.<sup>[19,20]</sup> Jang et al. and Aoshima et al. along with many others have since shown that the dissolution of Mn-ions is particularly high at higher charged state of LMO.<sup>[11,21]</sup> Wang et al. used a rotating ring-disk collection experiment to show that the concentration of dissolved  $\text{Mn}^{2+}$  into the electrolyte increases with cycle number and at elevated temperatures.<sup>[16]</sup> The dissolution is especially elevated at high state of charge (over 4.1 V vs.  $\text{Li}/\text{Li}^+$ ) and low state of charge (lower than 3.1 V vs.  $\text{Li}/\text{Li}^+$ ), specifically peaking at high state of charge.<sup>[21–25]</sup> In the investigation of LMOs storage performance,

[a] Y. Tesfamhret, Dr. H. Liu, Dr. Z. Chai, Assoc. Prof. E. Berg, Assoc. Prof. R. Younesi  
Department of Chemistry – Ångström Laboratory,  
Uppsala University,  
Box 538, 75121 Uppsala, Sweden  
E-mail: reza.younesi@kemi.uu.se

 Supporting information for this article is available on the WWW under <https://doi.org/10.1002/celec.202001496>

 © 2021 The Authors. ChemElectroChem published by Wiley-VCH GmbH. This is an open access article under the terms of the Creative Commons Attribution License, which permits use, distribution and reproduction in any medium, provided the original work is properly cited.

Inoue et al. and Sano et al. settled in a similar conclusion where a combination of high state of charge and elevated temperatures would result in capacity loss.<sup>[21,26]</sup> Water residue in the electrolyte was identified as the accelerator of Mn-ion dissolution. In particular for electrolytes containing LiPF<sub>6</sub> salt, which decomposes through a reaction with water to form HF.<sup>[10,14,27–29]</sup>

The dissolved Mn<sup>2+</sup> ions migrate to and deposit on the anode to gradually interfere with Li<sup>+</sup> intercalation and increase anode impedance, which contributes to an overall cycling performance degradation.<sup>[14,28,30–32]</sup> The formation of inactive Mn<sup>4+</sup>, which remains in solid phase, contributes to the impedance increase of LMO, emerging from loss of electrical contact with conducting additive as well as cathode electrolyte interphase (CEI) layer build up from electrolyte oxidation.<sup>[21,33–39]</sup> A recent paper from Aurbach et al. however, has proposed that it in fact is Mn<sup>3+</sup> which is the more prevalent soluble ion rather than Mn<sup>2+</sup> from the stated disproportionation reaction.<sup>[40]</sup>

Different approaches have been taken to counteract the process of TM dissolution, principally surface modification by thin film coating and doping. Thin film coatings passivate the LMO surface to reduce Mn dissolution and can be in the form of metal-oxides, -fluorides and -phosphates.<sup>[41–43]</sup> Passivation of LMO surface is crucial for prohibiting against acidic surroundings, such as HF attack. The coatings are usually prepared by atomic layer deposition (ALD), a relatively low temperature and self-limiting technique for conformal and uniform coatings. Bulk and surface metal ion dopants stabilize the crystalline phase and usually have an oxidation state of lower than 3+, such as Ni<sup>2+</sup>, Co<sup>2+</sup> and Li<sup>+</sup>.<sup>[44–48]</sup> Average valence of Mn is thus kept higher than 3.5, resulting in a lower Mn<sup>3+</sup> content. By decreasing the amount of Mn<sup>3+</sup>, which is susceptible to Jahn-Teller distortion, Mn dissolution is correspondingly decreased.

Here, a commonly used Al<sub>2</sub>O<sub>3</sub> thin film is coated on the surface of the model LMO cathode by ALD deposition technique in an attempt to suppress the Mn-ion dissolution. Inductively coupled plasma spectroscopy (ICP) based method is adapted to quantify the dissolved Mn-ions into the electrolyte in cells using either LiPF<sub>6</sub> or LiClO<sub>4</sub> based electrolytes. To understand the influence of counter electrode and cross-talk on the amount of Mn dissolution from the working electrode, two different types of counter electrodes, Li-metal or lithium iron phosphate (LFP), is used.<sup>[49]</sup>

## 2. Results and Discussion

The LMO powder was coated using the ALD technique, aiming for two different thickness of Al<sub>2</sub>O<sub>3</sub> coating layer as described in the experimental section. Pristine LMO (PLMO) and coated powder were analyzed using ICP-OES, XPS, and SEM (Figure S1 and S2 in supporting information). The elemental mapping of Al indicates a homogenous distribution of Al<sub>2</sub>O<sub>3</sub> coating on the LMO particles (Figure S2). ICP-OES results disclosed that rather than doubling the amount of Al and thereby Al<sub>2</sub>O<sub>3</sub> by increasing cycle number from 5 to 10 cycles, the amount of Al only increased by a factor of 1.62 (Table 1). This indicates that saturation may not have been reached in each pulsing ALD

**Table 1.** Quantitative analysis of the Al in PLMO and Al<sub>2</sub>O<sub>3</sub> coated LMO powder by ICP-OES. Presented values are quantified elemental wt%. Al, calculated according to sample size tested.

Sample	Name	wt.% of Al
Pristine (LMO)	PLMO	0.0016
5 cycle ALD (LMO)	5CLMO	0.0741
10 cycle ALD (LMO)	10CLMO	0.1204

cycle and a pulsing cycle did not correspond to one monolayer of Al<sub>2</sub>O<sub>3</sub>. However, the higher 0.1204 wt.% than 0.0741 wt.% of Al shows that deposited aluminum has increased and a thicker coating has been achieved. An impurity level amount of Al is detected in PLMO powder 0.0016 (wt.%). The results from qualitative analyses with XPS support the achievement of increasing thickness as well as homogenous Al<sub>2</sub>O<sub>3</sub> coating on the LMO particles (Figure S1). Thickness of the Al<sub>2</sub>O<sub>3</sub> coating can be estimated based on the amount of Al (quantified with ICP-OES, Table 1) and 1.85 m<sup>2</sup>/g BET surface area measured of the PLMO powder (Table S1 and S2). Thickness of Al<sub>2</sub>O<sub>3</sub> is estimated to be 0.31 nm and 0.19 nm for 10CLMO and 5CLMO, respectively.

Uncoated and coated LMO were cycled in half-cell using Li metal as counter electrode, as shown in Figure 1. The cells based on PLMO and 5CLMO with LiPF<sub>6</sub> containing electrolyte showed a comparable capacity retention of 95% and 91% from the initial charge capacities of 119 and 110 after 49 cycles, respectively. All Li||LMO display two plateaus which can be assigned to the two-stage intercalation/deintercalation process in spinel LMO. A higher overpotential is observed at 1C compared to C/5 (Figure 1 b and c). Dissolved Mn-ions have the possibility to diffuse through the separator and deposit on the Li-metal surface after being reduced to metallic Mn.<sup>[37–39]</sup> This gradually increases anode impedance. Hence, the amount of Mn in the electrolyte and the amount deposited on Li-metal counter electrode were quantified by ICP-OES (Figure 1 d and e). The amount of Mn is an order of magnitude higher on Li metal compared to that in the electrolyte for both PLMO and 5CLMO samples. This reveals that most dissolved Mn from LMO cathode move to and deposit on Li metal counter electrode. The total quantified Mn dissolved into the electrolyte as well as deposited on Li-metal surface is 0.493 wt.% and 0.552 wt.% for PLMO and 5CLMO, respectively. The capacity loss arising from the absence of the Mn-ions is thus lower compared to the capacity loss observed from electrochemical cycling of which was 5% and 9% for PLMO and 5CLMO, respectively. This indicates Mn-ion dissolution is not the sole justification of capacity loss, as it does not fully account for the loss of capacity. This means that the measured capacity loss is also accelerated by other phenomena as a consequence of Mn dissolution; deposition of migrated Mn on the anode, increase in cathode or anode resistance due to blockage of Li-ion intercalation/deintercalation sites, and structural changes on the cathode surface are possible mechanism leading to further capacity loss in addition to the loss due to Mn dissolution.<sup>[4,36]</sup>

To determine the influence of other possible parameters on Mn dissolution, we investigated the influence of the counter

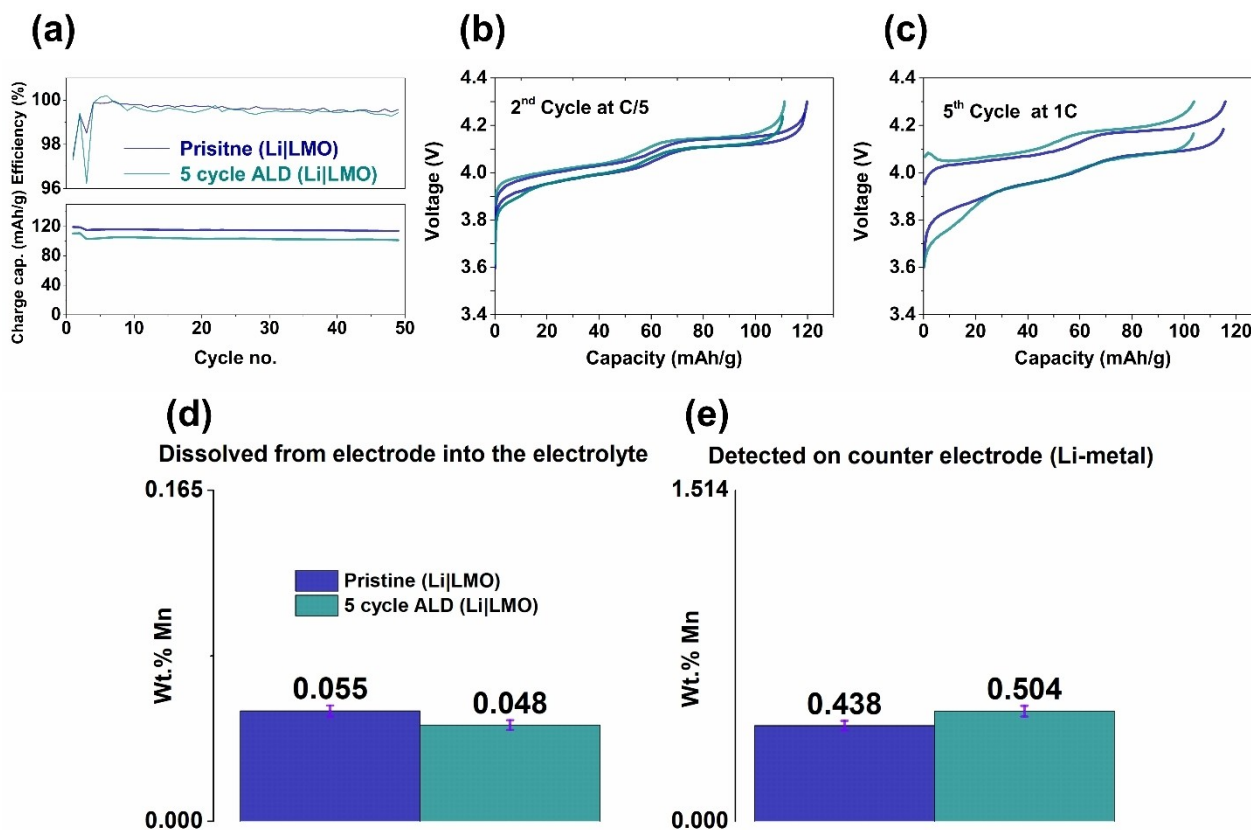


**Figure 1.** Cycle life of Li|LMO with LiPF<sub>6</sub>/EC/DEC electrolyte and relative Mn dissolution determination by ICP-OES. First two cycles at C/5 and the rest at 1 C, between 3.5 and 4.3 V vs. Li/Li<sup>+</sup>. (a) Capacity retention and coulombic efficiency over 49 cycles. (b) 2<sup>nd</sup> cycle at C/5. (c) 5<sup>th</sup> cycle at 1 C. (d) %Mn dissolution into the electrolyte from the cycled LMO electrodes in LMO|Li-metal cells. (e) %Mn dissolved from LMO electrode and deposited on Li-metal counter electrode.

electrode and electrolyte salt. As shown above that the dissolution of Mn-ions into the electrolyte leads to deposition on the surface of Li-metal, therefore, LFP (that has a high average potential of 3.45 V) was chosen as the counter electrode to restrict the reduction of Mn-ions on the surface of the anode. This maximizes the amount of dissolved Mn-ions available in the electrolyte making it optimum for the ICP-quantification analysis. Figure 2 shows galvanostatic cycling of LFP|LMO cells with two different electrolyte salts of LiPF<sub>6</sub> or LiClO<sub>4</sub> dissolved in EC:DEC. The cells were cycled between the voltage window of 0.2 V- 0.9 V (corresponding to 3.5 and 4.3 V vs. Li/Li<sup>+</sup>). LFP anode had previously undergone full delithiation followed by lithiation up to 33%. The cells were assembled with an anode to cathode capacity ratio of ~ 66:33 (0.9 mAh: 0.3 mAh). LFP counter electrode is constrained to a flat potential plateau (3.45 V) while relative LMO working electrode potential fluctuates during galvanostatic cycling, therefore, avoiding any possible LFP|LMO voltage slippage due to LFP.

After 49 cycles, the PLMO, 5CLMO and 10CLMO electrodes cycled with LiPF<sub>6</sub> containing electrolyte showed a comparable capacity retention of 80%, 87% and 79% from the initial charge capacities of 115, 118 and 108 mAh/g, respectively. The same trend can be observed for PLMO and 5CLMO electrodes cycled with LiClO<sub>4</sub> containing electrolyte, where no significant difference can be observed in cyclability. A capacity retention of 87%

and 81% from the initial capacities of 118 and 120 mAh/g for PLMO and 5CLMO electrodes, respectively. Therefore, the presence of Al<sub>2</sub>O<sub>3</sub> surface coating does not have a major contribution to an increase in capacity retention and Coulombic efficiency under these circumstances. Similar to Li|LMO, an expected higher overpotential when cycled at 1 C compared to C/5 can also be observed for all LFP|LMO cells (Figure 2 c and f).

The amount of Mn dissolved in the electrolyte was higher for both coated samples (5CLMO and 10CLMO) compared to that for non-coated sample (PLMO) for both studied electrolyte salts, see Figure 2 g and h. This is in contrast to the common belief the Al<sub>2</sub>O<sub>3</sub> coating is beneficial to suppress Mn dissolution. The results in Figure 2 g and h also show that the dissolution of Mn-ions into electrolyte from LFP|LMO is an order of magnitude higher compared to their Li|LMO counterparts. The total quantified Mn in the electrolyte and Li-metal surface for the cells based on PLMO was 0.493 wt.% Li|LMO, compared to 0.690 wt.% of its LFP|LMO counterpart (note: measurement only in the electrolyte for LFP|LMO). Similarly, the total quantified Mn for Li|5CLMO cell was 0.552 wt.% compared to 1.684 wt.% of its LFP|LMO counterpart. It is likely that the very reactive Li-metal surface reacted with traces of water and HF and effectively cleaned the electrolyte. Thus, the main cause of Mn-ion dissolution has been minimized.

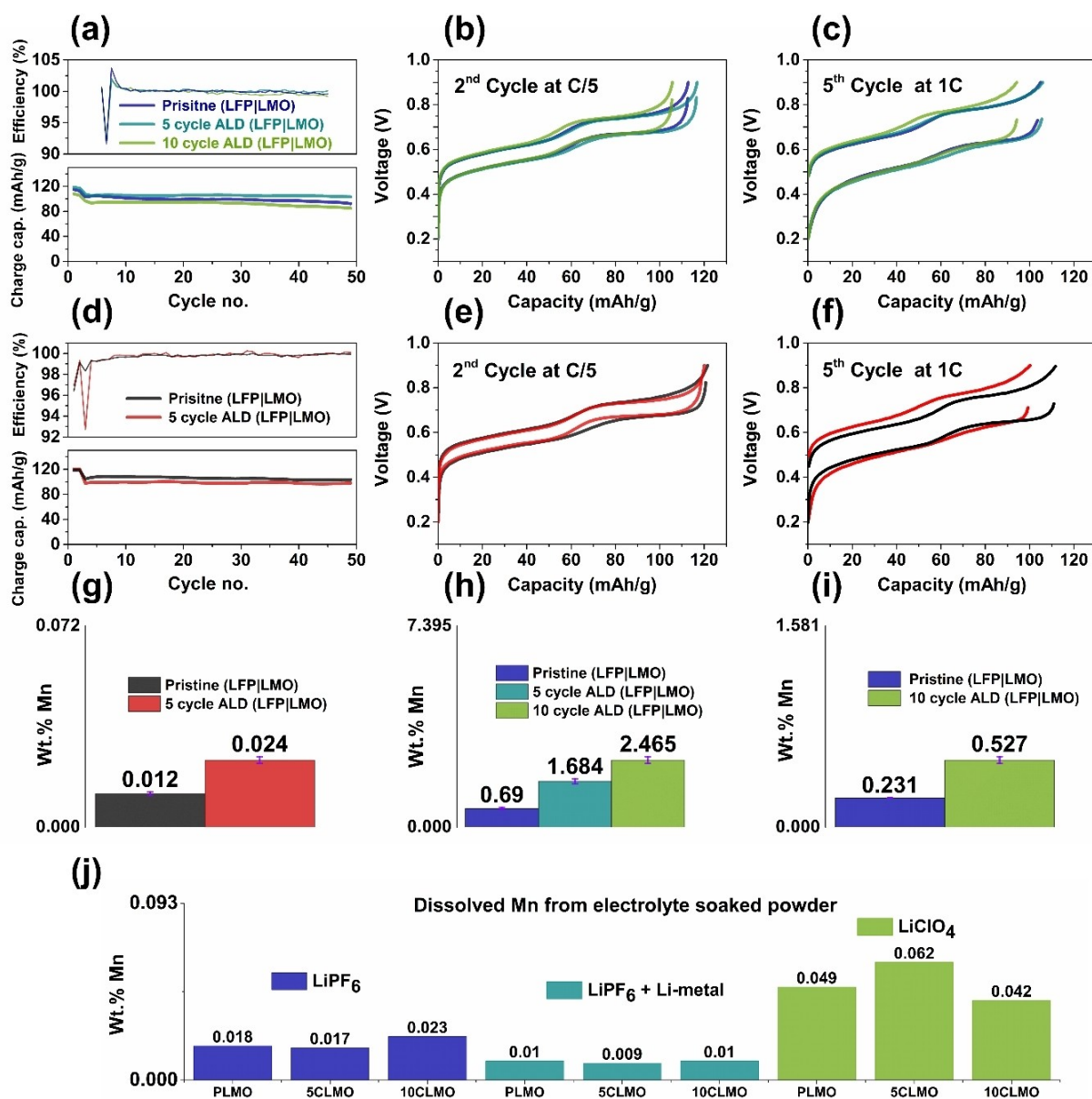


**Figure 2.** Galvanostatic cycling of LFP || LMO cells with LiPF<sub>6</sub> | EC | DEC and LiClO<sub>4</sub> | EC | DEC electrolytes and relative Mn dissolution determination by ICP-OES. First two cycles at C/5 and the rest at 1 C, between 0.2 and 0.9 V (corresponding to between 3.5 and 4.3 V vs. Li/Li<sup>+</sup>). (a) Capacity retention and Coulombic efficiency over 49 cycles (LiPF<sub>6</sub> salt). (b) 2<sup>nd</sup> cycle at C/5 (LiPF<sub>6</sub> salt). (c) 5<sup>th</sup> cycle at 1 C (LiPF<sub>6</sub> salt). (d) Capacity retention and coulombic efficiency over 49 cycles (LiClO<sub>4</sub> salt). (e) 2<sup>nd</sup> cycle at C/5 (LiClO<sub>4</sub> salt). (f) 5<sup>th</sup> cycle at 1 C (LiClO<sub>4</sub> salt). (g) %Mn dissolution into the electrolyte from the cycled LMO electrodes in LFP || LMO cells (LiClO<sub>4</sub> salt). (h) %Mn dissolution into the electrolyte from the cycled LMO electrodes in LFP || LMO cells (LiPF<sub>6</sub> salt). (i) %Mn dissolution into the electrolyte from LMO electrodes in LFP || LMO cells at OCV for the same amount of time as the cells (LiPF<sub>6</sub> salt). (j) Soaking test of Pristine, 5CLMO and 10CLMO powders in different electrolytes and chemical dissolution of Mn from powder into electrolyte, determined by ICP-OES. Powder was soaked in electrolyte for a week prior to ICP-OES measurements.

Symmetric-cells of LMO || LMO and 10CLMO || 10CLMO with LiPF<sub>6</sub> | EC | DEC electrolyte were also investigated for quantification of Mn dissolution, see Figure S5. After 49 cycles, PLMO and 10CLMO showed capacity retention of 32% and 56% from the initial charge capacities of 114 and 113, respectively. The substantial capacity loss compared to Li || LMO and LFP || LMO cells was attributed to issues that arise with alignment of electrodes with identical diameters during cell assembly of symmetric-cells in pouch bags. This would then lead to uneven current distribution at the electrode edges. Mn dissolution of

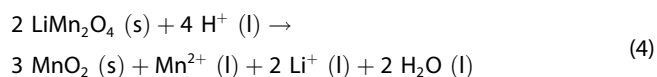
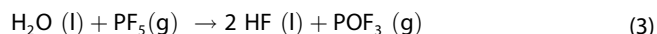
8.73 wt.% for 10CLMO compared to 13.99 wt.% for PLMO was detected from the total available Mn in both working and counter LMO electrodes in symmetric-cell setup.

The amount of dissolved Mn-ion into the electrolyte is two orders of magnitude higher for LFP || LMO cells with LiPF<sub>6</sub>-based electrolyte compared to that in LiClO<sub>4</sub> based electrolyte (Figure 2 g, h). Furthermore, a substantial amount of Mn-ion dissolution can be observed for non-cycled cells (i.e. no current/potential is applied and the cell was kept under relaxation for 90 hours) as reported in Figure 2 i. This indicates

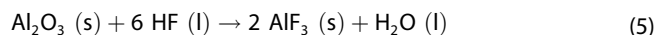
parasitic chemical -in addition to electrochemical reactions- leads to the dissolution of Mn. The amount of time of which the non-cycled cells are kept under relaxation corresponds to the same amount of time where the cycled cells are assembled and disassembled. Similar to Li || LMO, no correlation is observed between Mn dissolution from the LMO electrode and capacity fade, which demonstrates that not only does capacity fade result from redox active component loss, but also its resulting impact on the anode and cathode.<sup>[50]</sup>

PLMO, 5CLMO and 10CLMO powder were soaked in LiPF<sub>6</sub>|EC|DEC and LiClO<sub>4</sub>|EC|DEC electrolyte to investigate the chemical dissolution behavior of Mn (Figure 2 j). For comparison, LiPF<sub>6</sub>|EC|DEC electrolyte with added Li-metal (8 mg Li-metal per ml electrolyte) was investigated. Li-metal was stored in the electrolyte for a week before extraction. The Li-metal can potentially scavenge traces of H<sub>2</sub>O and HF, which based on the presented results have proven to be the root causes of dissolution. The ratio of electrolyte volume to LMO powder is kept 10 μl to 1 mg, respectively. This ratio is similar to the condition in the electrochemical cells (Figure 2 i). The chemical dissolution of Mn proved to be the lowest in the Li cleaned LiPF<sub>6</sub>|EC|DEC electrolyte, demonstrating the advantage of Li-metal. This conclusion coincides with the results from Li || LMO cells (Figure 1). Although dissolution is higher in standard LiPF<sub>6</sub>|EC|DEC electrolyte, LiClO<sub>4</sub>|EC|DEC showed the highest chemical dissolution. This can be explained by the oxidative properties of LiClO<sub>4</sub> salt. It should be highlighted that the amount of Mn detected in powder soaking tests is an order of magnitude lower compared to the electrochemical cell tests, approaching the lower detection limitations of ICP-OES. Thus, comparison of values that are very close to the limitations of the ICP-OES might be diffuse.

PLMO, 5CLMO and 10CLMO show a trend of increasing dissolution, in the mentioned order (Figure 2 h). It has been suggested that the presence of HF in the electrolyte can result in Mn-ion dissolution through reaction equation (4).<sup>[51]</sup> In LiPF<sub>6</sub> salt containing electrolytes, HF forms due to the reactions between the salt and traces of water according to reactions (2) and (3).<sup>[52,53]</sup>



The case of LMO with Al<sub>2</sub>O<sub>3</sub> coating showing higher dissolution compared to PLMO can be based on reaction equation (5), as illustrated in Figure 3. It is suggested that Al<sub>2</sub>O<sub>3</sub> can sequester HF and effectively act as a scavenger,<sup>[29,42,54]</sup> where water formed as a byproduct along with AlF<sub>3</sub>.



However, water has the possibility to further form HF and in turn increase Mn-ion dissolution,<sup>[29,55]</sup> which is contradictory to

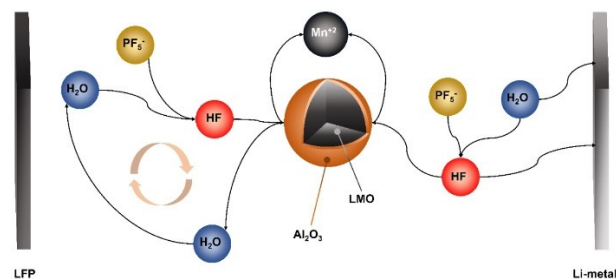


**Figure 3.** A schematic illustration of HF as a root cause for Mn-ion dissolution from a pristine LMO as well as Al<sub>2</sub>O<sub>3</sub> coated LMO. Al<sub>2</sub>O<sub>3</sub> coating in the presence of HF can form H<sub>2</sub>O, and consequently H<sub>2</sub>O leads to the hydrolysis of LiPF<sub>6</sub> to produce more HF. Li-metal counter electrode consumes impurities such as HF and H<sub>2</sub>O that lead to Mn dissolution in the electrolyte.

the onset purpose of the coating. Park et al<sup>[56]</sup> performed surface analysis on thin film lithium cobalt oxide (LCO) coated with Al<sub>2</sub>O<sub>3</sub> to explain this contradiction. They proposed Al<sub>2</sub>O<sub>3</sub> coating can transform to AlF<sub>3</sub>·3H<sub>2</sub>O layer during cycling, which would inhibit the further formation of HF by scavenging H<sub>2</sub>O molecules. The composition of possible functional groups on the surface sites of Al<sub>2</sub>O<sub>3</sub> is another factor which must also be considered as it could have an impact on LiPF<sub>6</sub> hydrolysis. Termination of the ALD deposition procedure with either TMA or H<sub>2</sub>O yields to methyl (CH<sub>3</sub>) or hydroxyl (OH) groups on the surface, respectively. Protons arising from those functional groups have the possibility to participate and substantially favor the dissociation of PF<sub>6</sub><sup>-</sup>, with HF and PF<sub>5</sub> as reaction products.<sup>[57]</sup> In this work, the deposition process was terminated with TMA, so further research is required to verify whether similar behavior is observed with water termination.

### 3. Conclusion

A comparative quantification of Mn dissolution from LMO cathode materials based on ICP-OES measurements is discussed in this work. The substantially higher dissolution of Mn in LFP || LMO cells containing LiPF<sub>6</sub> compared to LiClO<sub>4</sub> based electrolytes implies HF is the root cause of dissolution. The observed Mn dissolution in non-cycled cells indicates that HF generated dissolution is not only due to electrochemical but also a parasitic chemical reaction. However, the amount of dissolved Mn due to chemical reactions is substantially lower than that due to electrochemical reactions. Concentration of Mn-ions in the electrolyte is lower in LMO || Li in comparison to LFP || LMO cells. This is attributed to the migration and deposition of Mn-ions on the Li-metal surface, due to the significantly lower potential of Li-metal counter electrode compared to LFP. This is clearly observed with the substantial amount of Mn detected on the Li-metal counter electrodes by ICP-OES. The total quantified Mn in the electrolyte and Li-metal surface of LMO || Li cells is still less compared to the Mn detected in the electrolyte of LFP || LMO cells. This is likely because Li-metal reacts and consumes impurities such as HF and H<sub>2</sub>O that lead to Mn dissolution in the electrolyte and minimizes the dissolution

process.  $\text{Al}_2\text{O}_3$ -coated LMO showed higher dissolution in LFP|LMO and Li||LMO configuration compared to uncoated LMO, which is an unexpected finding, contradictory to the purpose of the protective  $\text{Al}_2\text{O}_3$  thin film coating proposed in literatures. This can be explained by  $\text{Al}_2\text{O}_3$  in the presence of HF can form  $\text{H}_2\text{O}$ , and consequently  $\text{H}_2\text{O}$  leads to the hydrolysis of  $\text{LiPF}_6$  to produce more HF. Therefore, uncoated sample can show lower amount of Mn dissolution compared to  $\text{Al}_2\text{O}_3$ -coated sample when HF is present in the electrolyte.

## Experimental Section

### ALD of $\text{Al}_2\text{O}_3$

PICOSUN® R-200 Standard ALD system was used to deposit  $\text{Al}_2\text{O}_3$  directly on LMO powder (SEDEMA). Deposition process was performed at  $120^\circ\text{C}$ .  $\text{N}_2$  gas was selected as a carrier gas for Trimethylaluminum (TMA) and water precursors. One complete ALD deposition cycle can be described as following: i) TMA was pulsed for 0.2 sec at a flow rate of 15 sccm into the ALD reactor chamber (where the substrate, LMO powder, is situated), followed by a purge with the carrier gas, at a flow rate of 100 sccm. This step was repeated 10 times to achieve a net TMA pulsing time of 2 sec. ii) Reactor was purged with carrier gas for 60 sec at flow rate of 600 sccm. iii) water was pulsed for 0.2 sec at a flow rate of 15 sccm followed by purging with carrier gas at a flow rate of 100 sccm. This step was repeated 10 times to achieve a net water pulsing time of 2 sec. iv) Reactor was purged by carrier gas for 60 sec at flow rate of 600 sccm. The described steps complete one ALD deposition cycle. LMO samples with 5 and 10 ALD deposition cycles of  $\text{Al}_2\text{O}_3$  were prepared and labeled 5CLMO and 10CLMO, respectively.

### Electrode Preparation

Identical electrode preparation process was used for pristine LMO, 5CLMO and 10CLMO. Slurry containing LMO powder (pristine/5CLMO/10CLMO, 90 wt%), carbon black (Imerys, C65, 5 wt%) and PVdF binder (5 wt%, PVdF–HFP, Kynar Flex 2801) in N-methyl-2-pyrrolidone (NMP, VWR) was homogenized in Retch MM 4400 ball miller for 1 hr (25 Hz). Binder was previously prepared as a 6 wt. % PVdF and 94 wt. % NMP solution. Slurry was composed of 70 wt. % liquid and 30 wt. % solid content. Slurry was then casted on a carbon coated Al-foil (20  $\mu\text{m}$  thickness), wherein a coating gap of the film applicator was set to 200  $\mu\text{m}$ . The resulting active mass loading was around 5  $\text{mg}/\text{cm}^2$  or 0.6  $\text{mAh}/\text{cm}^2$  (calculated based on the 120  $\text{mAh}/\text{g}$  practical capacity of LMO). The coating was dried at  $70^\circ\text{C}$  in standard atmosphere and perforated into either 8 mm or 10 mm diameter electrodes. Similarly, slurry containing LFP powder (LIFE POWER P2, 85 wt%), carbon black (Imerys, C65, 10 wt%) and PVdF binder (5 wt%, PVdF–HFP, Kynar Flex 2801) in NMP (VWR) was homogenized in PM100 ball miller for 1 hr (350 rpm). Binder correspondingly introduced in a solution form of 6 wt. % PVdF and 94 wt. % NMP. Slurry was composed of 70 wt. % liquid and 30 wt. % solid content. The resulting active mass loading was around 5  $\text{mg}/\text{cm}^2$  or 0.675  $\text{mAh}/\text{cm}^2$  (calculated based on the 150  $\text{mAh}/\text{g}$  practical capacity of LFP). The coating was dried at  $70^\circ\text{C}$  in standard atmosphere and perforated into 13 mm diameter electrodes. All electrodes were dried under vacuum at  $120^\circ\text{C}$  for 12 h before utilization.

### Cell Assembly

Figure 4 shows a schematic of how the Li||LMO, symmetric cells (LMO||LMO) and LFP|LMO look. Four separators were used, of which the two outer are Celgard (2325,  $2 \times 2$  cm) and two inner are glass fiber (Whatman, grade GF/A, 20 mm diameter). The Celgard and glass fiber separators were dried for 12 h under vacuum at temperatures  $70^\circ\text{C}$  and  $120^\circ\text{C}$ , respectively. Aluminum current collectors were used for the LMO and LFP electrodes and nickel was used for Li-metal electrodes. In Li||LMO, the lithium counter electrode diameter was 15 mm. All cells were assembled in a  $5 \times 5$  cm pouch bag format in an Argon filled glovebox.

The LFP electrodes were fully delithiated and then lithiated 33% in a separate pouch Li||LMO in which 15 mm Li-metal counter electrode,  $2 \times 2$  cm Celgard (2325) and 100  $\mu\text{L}$  of either of the two previously mentioned electrolytes were used. In three-electrode cells (Figure 1b), a small Li-metal piece between two Celgard separators was used as a reference electrode.

### Electrochemical Characterization

All galvanostatic cycling tests were performed on LANDT battery testing system (model CT2001 A), at room temperature ( $20\text{--}22^\circ\text{C}$ ). The cells were kept at OCV for 5 h prior cycling. The first two cycles were run at C/5 and the rest at 1 C. C-rate was calculated based on the 148  $\text{mAh}/\text{g}$  theoretical capacity of LMO. Li||LMO were cycled between 3 V and 4.3 V. Symmetric cells were cycled between cell voltages of  $-0.6$  and 0.6 V. LFP|LMO cell were cycled between cell voltages of 0.2 V and 0.9 V. Arbin laboratory battery cycling system was used for cycling testing three-electrode cells, at room temperature ( $20\text{--}22^\circ\text{C}$ ).

ICP. The electrolyte volume for each cell was fixed to 250  $\mu\text{L}$  of either  $\text{LiPF}_6|\text{EC}|\text{DEC}$  or  $\text{LiClO}_4|\text{EC}|\text{DEC}$ . 1 M  $\text{LiPF}_6$  in EC:DEC (1:1 vol.%) 99.9% was provided from Solvionics.  $\text{LiClO}_4|\text{EC}|\text{DEC}$  electrolyte was prepared by mixing 1:1 vol.% ethylene carbonate (EC, BASF) and diethylene carbonate (DEC, BASF). Lithium perchlorate ( $\text{LiClO}_4$ , Sigma Aldrich, 99.9%) was dried at  $120^\circ\text{C}$  for 24 h under vacuum, then added to the EC|DEC solvent solution to form 1 M electrolyte.

The glass fiber separators, with the thickness of 1.6  $\mu\text{m}$ , can hold enough electrolyte which can be extracted post cycling in order to analyze by ICP-OES. The outer Celgard separators have the function of protection from contamination from the working and counter electrodes, during extraction of the post-cycled electrolyte. The withdrawn glass fiber separators containing post-cycled electrolyte were inserted into a 2 mL epindorf centrifugation tubes (VWR) and centrifuged for 10 mins, using VWR 2000 rpm centrifuge. The glass fibers were fastened in the top of the epindorf, thus the electrolyte was extracted to the bottom after centrifugation. 100  $\mu\text{L}$  of the extracted electrolyte was sampled for ICP-OES analysis for each cell.

The sampled electrolyte was digested with Nitric acid (Nitric acid 65%, VWR) over 16 h and diluted 1000\* by milli Q water. Avio 500

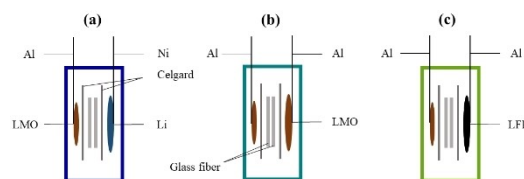


**Figure 4.** Schematic illustration of (a) Li||LMO, (b) Symmetric cell (LMO||LMO) and (c) LFP|LMO configuration.

Scott/Cross-Flow Configuration was used for ICP measurements. ICP-OES was calibrated with concentration of 10, 5, 1, 0.5, 0.1 and 0.05  $\mu\text{g/mL}$  of Manganese provided from Multi-element Calibration Standard (Perkin Elmer). ICP quantification was performed on LMO powder and different electrolytes. Al content was quantified on ALD coated and pristine LMO and results are presented in percentage based on the tested powder weight in order to standardize, rather than in ppm as the powder weights vary. Similarly, the results of dissolved Mn quantified in electrolytes is presented in weight percentage based on the available Mn in assembled LMO electrodes (the raw data and detail values for ICP-OES measurements are provided in Table S3 and S4).

### Surface Characterization

SEM images were taken using Zeiss/LEO 1550, and the Raman spectra were obtained using Renishaw inVia Raman Microscope with a laser source of 532 nm. EDS-detector mounted on the same SEM instrument was used for surface mapping and line-scan characterization. XRD diffractograms were attained using Siemens Bragg-Brentano D5000.

### X-ray Photoelectron Spectroscopy (XPS)

The sample preparation was the same as for SEM except that an airtight transfer system was used for sample to avoid any exposure to air. All samples were analyzed using a Phi-5500 instrument with monochromatized Al K $\alpha$  radiation (1486.6 eV).

### Transmission Electron Microscopy (TEM)

High-angle annular dark-field (HAADF) imaging with scanning TEM (STEM) mode, and energy dispersive X-ray spectroscopy (EDX) was done on a FEI Titan Themis 200 microscope and a SuperX X-ray detector.

### Acknowledgements

The authors acknowledge Assoc. Prof. Erik Lewin for access to an ALD reactor and Dr. Mårten Rooth for scientific discussions regarding ALD coatings. We also acknowledge financial support from the Swedish Energy Agency via project no. 45518-1 and via StandUp for Energy.

### Conflict of Interest

The authors declare no conflict of interest.

**Keywords:** ageing · ALD · hydrogen fluoride · spinel · transition metal

- [1] V. Etacheri, R. Marom, R. Elazari, G. Salitra, D. Aurbach, *Energy Environ. Sci.* **2011**, *4*, 3243.
- [2] E. J. Berg, C. Villevieille, D. Streich, S. Trabesinger, P. Novák, *J. Electrochem. Soc.* **2015**, *162*, A2468–A2475.
- [3] M. Wohlfahrt-Mehrens, C. Vogler, J. Garche, in *J. Power Sources*, Elsevier, **2004**, pp. 58–64.
- [4] C. Zhan, T. Wu, J. Lu, K. Amine, *Energy Environ. Sci.* **2018**, *11*, 243–257.

- [5] T. Nordh, R. Younesi, M. Hahlin, R. F. Duarte, C. Tengstedt, D. Brandell, K. Edström, *J. Phys. Chem. C* **2016**, *120*, 3206–3213.
- [6] W. W. Liu, D. Wang, Z. Wang, J. Deng, W. M. Lau, Y. Zhang, *Phys. Chem. Chem. Phys.* **2017**, *19*, 6481–6486.
- [7] S. Dou, *Ionics* **2015**, *21*, 3001–3030.
- [8] A. Van Der Ven, C. Marianetti, D. Morgan, G. Ceder, *Solid State Ionics* **2000**, *135*, 21–32.
- [9] Y. Kim, J. Lim, S. Kang, *Int. J. Quantum Chem.* **2013**, *113*, 148–154.
- [10] P. Arora, R. E. White, M. Doyle, *J. Electrochem. Soc.* **1998**, *145*, 3647–3667.
- [11] T. Aoshima, K. Okahara, C. Kiyohara, K. Shizuka, *J. Power Sources* **2001**, *97–98*, 377–380.
- [12] Y. Dai, L. Cai, R. E. White, *J. Electrochem. Soc.* **2013**, *160*, A182–A190.
- [13] Y. Xia, Y. Zhou, M. Yoshio, *J. Electrochem. Soc.* **1997**, *144*, 2593–2600.
- [14] J. Lu, K. S. Lee, *Mater. Technol.* **2016**, *31*, 628–641.
- [15] M. M. Thackeray, W. I. F. David, P. G. Bruce, J. B. Goodenough, *Materials Research Bulletin* **1983**, *18*, 461–472.
- [16] X. Li, Y. Xu, C. Wang, *J. Alloys Compd.* **2009**, *479*, 310–313.
- [17] A. Yamada, *J. Solid State Chem.* **1996**, *122*, 160–165.
- [18] S. R. Das, S. B. Majumder, R. S. Katiyar, *J. Power Sources* **2005**, *139*, 261–268.
- [19] C. H. Lu, S. W. Lin, *J. Mater. Res.* **2002**, *17*, 1476–1481.
- [20] J. M. Tarascon, D. Guyomard, *Electrochim. Acta* **1993**, *38*, 1221–1231.
- [21] L. Cai, Y. Dai, M. Nicholson, R. E. White, K. Jagannathan, G. Bhatia, *J. Power Sources* **2013**, *221*, 191–200.
- [22] A. Du Pasquier, A. Blyer, P. Courjal, D. Larcher, G. Amatucci, B. Gérard, J. M. Tarascon, *J. Electrochem. Soc.* **1999**, *146*, 428–436.
- [23] G. G. Amatucci, A. Blyer, C. Sigala, P. Alfonso, J. M. Tarascon, *Solid State Ionics* **1997**, *104*, 13–25.
- [24] K. Nishimura, T. Douzono, M. Kasai, H. Andou, Y. Muranaka, Y. Kozono, *J. Power Sources* **1999**, *81–82*, 420–424.
- [25] A. Antonini, C. Bellitto, M. Pasquali, G. Pistoia, *J. Electrochem. Soc.* **1998**, *145*, 2726–2732.
- [26] T. Inoue, M. Sano, *J. Electrochem. Soc.* **1998**, *145*, 3704–3707.
- [27] L. Baggetto, N. J. Dudney, G. M. Veith, *Electrochim. Acta* **2013**, *90*, 135–147.
- [28] G. Xu, Z. Liu, C. Zhang, G. Cui, L. Chen, *J. Mater. Chem. A* **2015**, *3*, 4092–4123.
- [29] G. H. Waller, P. D. Brooke, B. H. Rainwater, S. Y. Lai, R. Hu, Y. Ding, F. M. Alamgir, K. H. Sandhage, M. L. Liu, *J. Power Sources* **2016**, *306*, 162–170.
- [30] J. Wandt, A. Freiberg, R. Thomas, Y. Gorlin, A. Siebel, R. Jung, H. A. Gasteiger, M. Tromp, *J. Mater. Chem. A* **2016**, *4*, 18300–18305.
- [31] C. Zhan, X. Qiu, J. Lu, K. Amine, *Adv. Mater. Interfaces* **2016**, *3*, 1500856.
- [32] Z. Chen, Y. Qin, K. Amine, Y. K. Sun, *J. Mater. Chem.* **2010**, *20*, 7606–7612.
- [33] J. Vetter, P. Novák, M. R. Wagner, C. Veit, K.-C. Möller, J. O. Besenhard, M. Winter, M. Wohlfahrt-Mehrens, C. Vogler, A. Hammouche, *J. Power Sources* **2005**, *147*, 269–281.
- [34] T. Liu, A. Dai, J. Lu, Y. Yuan, Y. Xiao, L. Yu, M. Li, J. Gim, L. Ma, J. Liu, et al., *Nat. Commun.* **2019**, *10*, DOI 10.1038/s41467-019-12626-3.
- [35] D. H. Jang, Y. J. Shin, S. M. Oh, *J. Electrochem. Soc.* **1996**, *143*, 2204–2211.
- [36] D. Aurbach, M. D. Levi, K. Gamulski, B. Markovsky, G. Salitra, E. Levi, U. Heider, L. Heider, R. Oesten, *J. Power Sources* **1999**, *81–82*, 472–479.
- [37] W. Choi, A. Manthiram, *J. Electrochem. Soc.* **2006**, *153*, A1760.
- [38] A. Blyer, A. Du Pasquier, G. Amatucci, J. M. Tarascon, *Ionics* **1997**, *3*, 321–331.
- [39] I. A. Shkrob, A. J. Kropf, T. W. Marin, Y. Li, O. G. Poluektov, J. Niklas, D. P. Abraham, *J. Phys. Chem. C* **2014**, *118*, 24335–24348.
- [40] A. Banerjee, Y. Shilina, B. Ziv, J. M. Ziegelbauer, S. Luski, D. Aurbach, I. C. Halalay, *J. Am. Chem. Soc.* **2017**, *139*, 1738–1741.
- [41] F. Mattelaer, P. M. Vereecken, J. Dendooven, C. Detavernier, *Adv. Mater. Interfaces* **2017**, *4*, 1601237.
- [42] Z. Chen, Y. Qin, K. Amine, Y.-K. Sun, *J. Mater. Chem.* **2010**, *20*, 7606.
- [43] X. Xiao, P. Lu, D. Ahn, *Adv. Mater.* **2011**, *23*, 3911–3915.
- [44] Q. Liu, S. Wang, H. Tan, Z. Yang, J. Zeng, *Energies* **2013**, *6*, 1718–1730.
- [45] Y. J. Wei, L. Y. Yan, C. Z. Wang, X. G. Xu, F. Wu, G. Chen, *J. Phys. Chem. B* **2004**, *108*, 18547–18551.
- [46] L. Chen, R. E. Warburton, K. S. Chen, J. A. Libera, C. Johnson, Z. Yang, M. C. Hersam, J. P. Greeley, J. W. Elam, *Chem* **2018**, *4*, 2418–2435.
- [47] M. J. Young, S. Letourneau, R. E. Warburton, W. M. Dose, C. Johnson, J. Greeley, J. W. Elam, *J. Phys. Chem. C* **2019**, *123*, 23783–23790.
- [48] R. Younesi, S. Malmgren, K. Edström, S. Tan, *J. Solid State Electrochem.* **2014**, *18*, 2157–2166.
- [49] E. Björklund, D. Brandell, M. Hahlin, K. Edström, R. Younesi, *J. Electrochem. Soc.* **2017**, *164*, A3054–A3059.

- [50] C. Sångeland, R. Mogensen, D. Brandell, J. Mindemark, *ACS Appl. Polym. Mater.* **2019**, *1*, 825–832.
- [51] A. Bhandari, J. Bhattacharya, *J. Electrochem. Soc.* **2017**, *164*, A106–A127.
- [52] S. F. Lux, I. T. Lucas, E. Pollak, S. Passerini, M. Winter, R. Kostecki, *Electrochem. Commun.* **2012**, *14*, 47–50.
- [53] A. V. Plakhotnyk, L. Ernst, R. Schmutzler, *J. Fluorine Chem.* **2005**, *126*, 27–31.
- [54] S. T. Myung, K. Izumi, S. Komaba, Y. K. Sun, H. Yashiro, N. Kumagai, *Chem. Mater.* **2005**, *17*, 3695–3704.
- [55] M. T. F. Rodrigues, C. Liao, K. Kalaga, I. A. Shkrob, D. P. Abraham, *ACS Appl. Mater. Interfaces* **2019**, *2*, 5380–5385.
- [56] Y. Oh, D. Ahn, S. Nam, B. Park, *J. Solid State Electrochem.* **2010**, *14*, 1235–1240.
- [57] S. Solchenbach, M. Metzger, M. Egawa, H. Beyer, H. A. Gasteiger, *J. Electrochem. Soc.* **2018**, *165*, 3022–3028.

Manuscript received: November 24, 2020

Revised manuscript received: January 19, 2021

Accepted manuscript online: February 5, 2021